The young embedded disk L1527 IRS: constraints on the water snowline and cosmic-ray ionization rate from HCO+ observations

Hoff, M.L.R. van 't; Leemker, M.; Tobin, J.J.; Harsono, D.; Jørgensen, J.K.; Bergin, E.A.

The Astrophysical Journal, 932:6 (15pp), 2022 June 10 https://doi.org/10.3847/1538-4357/ac63b4

The Young Embedded Disk L1527 IRS: Constraints on the Water Snowline and Cosmic-Ray Ionization Rate from HCO+ Observations

Merel L. R. van 't Hoff[1], Margot Leemker[2], John J. Tobin[3], Daniel Harsono[4,6], Jes K. Jørgensen[5], and Edwin A. Bergin[1]
[1] Department of Astronomy, University of Michigan, 1085 S. University Ave., Ann Arbor, MI 48109-1107, USA; mervth@umich.edu
[2] Leiden Observatory, Leiden University, P.O. Box 9513, 2300 RA Leiden, The Netherlands
[3] National Radio Astronomy Observatory, 520 Edgemont Rd., Charlottesville, VA 22903, USA
[4] Institute of Astronomy and Astrophysics, Academia Sinica, P.O. Box 23-141, Taipei 106, Taiwan
[5] Niels Bohr Institute, University of Copenhagen, Øster Voldgade 5-7, DK-1350 Copenhagen K., Denmark
[6] Institute of Astronomy, Department of Physics, National Tsing Hua University, No. 101, Section 2, Kuang-Fu Road, Hsinchu 30013, Taiwan
Received 2022 February 18; revised 2022 March 31; accepted 2022 March 31; published 2022 June 8

Abstract

The water snowline in circumstellar disks is a crucial component in planet formation, but direct observational constraints on its location remain sparse owing to the difficulty of observing water in both young embedded and mature protoplanetary disks. Chemical imaging provides an alternative route to locate the snowline, and HCO^+ isotopologues have been shown to be good tracers in protostellar envelopes and Herbig disks. Here we present $\sim 0\farcs5$ resolution ($\sim$35 au radius) Atacama Large Millimeter/submillimeter Array (ALMA) observations of HCO^+ $J = 4 - 3$ and $H^{13}CO^+$ $J = 3 - 2$ toward the young (Class 0/I) disk L1527 IRS. Using a source-specific physical model with the midplane snowline at 3.4 au and a small chemical network, we are able to reproduce the HCO^+ and $H^{13}CO^+$ emission, but for HCO^+ only when the cosmic-ray ionization rate is lowered to 10^{-18} s^{-1}. Even though the observations are not sensitive to the expected HCO^+ abundance drop across the snowline, the reduction in HCO^+ above the snow surface and the global temperature structure allow us to constrain a snowline location between 1.8 and 4.1 au. Deep observations are required to eliminate the envelope contribution to the emission and to derive more stringent constraints on the snowline location. Locating the snowline in young disks directly with observations of H_2O isotopologues may therefore still be an alternative option. With a direct snowline measurement, HCO^+ will be able to provide constraints on the ionization rate.

Unified Astronomy Thesaurus concepts: Interstellar molecules (849); Astrochemistry (75); Protostars (1302)

1. Introduction

Evidence for an early start of planet formation, when the disk is still embedded in its envelope, has been accumulating. For example, rings in continuum emission that are ubiquitously observed toward Class II protoplanetary disks (e.g., Andrews et al. 2018) and could be a signpost of forming planets (e.g., Bryden et al. 1999; Zhu et al. 2014; Dong et al. 2018) are now also observed in disks as young as only $\sim$0.5 Myr (ALMA Partnership et al. 2015; Segura-Cox et al. 2020; Sheehan et al. 2020). Evidence for grain growth beyond interstellar medium (ISM) sizes has been inferred from low dust opacity spectral indexes in Class 0 sources (Kwon et al. 2009; Shirley et al. 2011), dust polarization (e.g., Kataoka et al. 2015, 2016; Yang et al. 2016), decreasing dust masses derived from (sub) millimeter observations for more evolved systems (e.g., Tychoniec et al. 2020), and CO isotopologue emission (Harsono et al. 2018). In addition, outflows present in this early phase may provide a way to overcome the radial drift barrier (Tsukamoto et al. 2021).

One of the key parameters in planet formation models is the location of the water snowline, that is, the disk midplane radius at which water molecules freeze out onto the dust grains. At this location, the growth of dust grains, and thus the planet formation efficiency, is expected to be significantly enhanced through triggering of the streaming instability (e.g., Stevenson & Lunine 1988; Drążkowska & Alibert 2017; Schoonenberg & Ormel 2017). In addition, since water is the dominant carrier of oxygen, the elemental carbon-to-oxygen (C/O) ratio of the planet-forming material changes across the water snowline (Öberg et al. 2011; Eistrup et al. 2018). Lichtenberg et al. (2021) illustrated the importance of the snowline location during disk evolution, as migration of the snowline may be an explanation for the isotopic dichotomy of solar system meteorites (e.g., Leya et al. 2008; Trinquier et al. 2009; Kruijer et al. 2017). In a different perspective, theoretical studies have shown that the position of the water snowline depends on the disk viscosity and dust opacity (Davis 2005; Lecar et al. 2006; Garaud & Lin 2007; Oka et al. 2011); hence, snowline measurements will provide important information for disk evolution models. Overall, observational constraints on the snowline location are thus crucial to understand planet formation and its outcome, and observations of young disks are particularly important, as they represent the earliest stages in planet formation.

Unfortunately, water emission is difficult to detect in both young and more evolved disks (Du et al. 2017; Notsu et al. 2018, 2019; Harsono et al. 2020), and thus determining the exact location of the snowline is challenging. However, observations of protostellar envelopes have shown that $H^{13}CO^+$ can be used as an indirect chemical tracer of the water snowline (Jørgensen et al. 2013; van 't Hoff et al. 2018a; Hsieh et al. 2019; van 't Hoff et al. 2022). This is based on gaseous water being the most abundant destroyer of HCO^+ in

warm dense gas around young stars. HCO^+ is therefore expected to be abundant only in the region where water is frozen out and gaseous CO is available for its formation (Phillips et al. 1992; Bergin et al. 1998). The high optical depth of the main isotopologue, HCO^+, impedes snowline measurements in protostellar envelopes (van 't Hoff et al. 2022), warranting the use of the less abundant isotopologues $H^{13}CO^+$ or $HC^{18}O^+$. Modeling of HCO^+ emission from Herbig disks has shown that this optical depth problem is partly mitigated in disks owing to their Keplerian velocity pattern, as different velocities trace different radii (Leemker et al. 2021).

Here we present Atacama Large Millimeter/submillimeter Array (ALMA) observations of HCO^+ and $H^{13}CO^+$ in the young disk L1527 IRS (also known as IRAS 04368+2557 and hereafter referred to as L1527). This well-studied Class 0/I protostar located in the Taurus molecular cloud (142 pc, Gaia Collaboration et al. 2021; Krolikowski et al. 2021) is surrounded by a 75–125 au Keplerian disk (Tobin et al. 2012, 2013; Aso et al. 2017) that is viewed nearly edge-on (Tobin et al. 2008; Oya et al. 2015) and is embedded in an extended envelope (e.g., Ohashi et al. 1997; Tobin et al. 2008). The observations are described and presented in Sections 2 and 3, respectively. In Section 4 we use the physical structure for L1527 derived by Tobin et al. (2013) to model the HCO^+ abundance and HCO^+ and $H^{13}CO^+$ emission, incorporating the HCO^+ abundance through either simple parameterization (Section 4.1) or the use of a small chemical network (Section 4.2). In Section 5.1 we then use the chemical modeling results to constrain the water snowline location in L1527. Finally, we discuss the cosmic-ray (CR) ionization rate in Section 5.2 and summarize the main conclusions in Section 6.

2. Observations

L1527 was observed with ALMA in HCO^+ on 2014 June 14 (project code 2012.1.00346.S; PI: N. Evans) for a total on-source time of 11 minutes. These observations were carried out using 33 antennas sampling baselines up to 650 m. The correlator setup consisted of four 234 MHz spectral windows, including one targeting the HCO^+ $J = 4 - 3$ transition at 356.734223 GHz, with 61 kHz ($\sim$0.05 km s^{-1}) spectral resolution.

In addition, L1527 was observed in $H^{13}CO^+$ on 2015 August 11 and 12 and September 2 (project code 2012.1.00193.S; PI: J.J. Tobin) for a total of 43 minutes on source per execution ($\sim$2.2 hr total). The observations were carried out with 42, 44, and 34 antennas for the three respective observing dates and sampled baselines up to 1.6 km. The correlator setup contained two 117 MHz spectral windows, including one targeting the $H^{13}CO^+$ $J = 3 - 2$ transition at 260.255339 GHz, with 31 kHz ($\sim$0.05 km s^{-1}) spectral resolution and two 2 GHz spectral windows with 15.6 MHz resolution, aimed for continuum measurements.

Calibration, self-calibration, and imaging of the HCO^+ and $H^{13}CO^+$ data sets were done using versions 4.2.1 and 4.3.1 of the Common Astronomy Software Application (CASA; McMullin et al. 2007), respectively, where the HCO^+ data were calibrated using the ALMA pipeline. For the HCO^+ observations, J0510+1800 was used as bandpass, phase, and flux calibrator. For the $H^{13}CO^+$ observations, the bandpass calibrator was J0423–0120, the flux calibrator was J0423–0130, and the phase calibrator was J0510+1800 for the August observations and J0440+2728 for the September observations. Both lines are imaged at a spectral resolution of 0.1 km s^{-1}. A *uv* taper of 500 kλ was applied to increase the signal-to-noise ratio of the $H^{13}CO^+$ image cube. The restoring beam is $0\farcs50 \times 0\farcs30$ (PA $= -3\fdg2$) for HCO^+ and $0\farcs47 \times 0\farcs28$ ($44\fdg7$) for $H^{13}CO^+$, and the images have an rms of 20 and 3.9 mJy beam^{-1} channel^{-1}, respectively. The maximum recoverable scale is $2\farcs7$ (380 au) for the HCO^+ observations and $2\farcs0$ (280 au) for $H^{13}CO^+$, that is, spanning the disk (75–125 au; Tobin et al. 2012, 2013; Aso et al. 2017) and innermost envelope.

3. Results

Figure 1 (top panels) presents the integrated intensity maps for HCO^+ $J = 4 - 3$ and $H^{13}CO^+$ $J = 3 - 2$ toward L1527. Emission from channels near the systemic velocity ($\Delta v \leqslant |0.5|$ km s^{-1}), where most of the emission is resolved out, is omitted. Both molecules display emission elongated along the north–south direction, that is, along the major axis of the edge-on disk, with the blueshifted emission south of the protostar. The HCO^+ emission is radially more compact than the $H^{13}CO^+$ emission, likely because the $J = 4 - 3$ transition traces warmer and denser material than the $J = 3 - 2$ transition. The higher sensitivity of the $H^{13}CO^+$ observations and more resolved-out emission for the optically thicker HCO^+ emission possibly play a role as well. For both lines, a central depression is visible, which at first thought may be interpreted as a lack of HCO^+ and $H^{13}CO^+$ in the inner region of the disk. However, modeling of HCO^+ emission by Hsieh et al. (2019) showed that a ring-shaped distribution of HCO^+ molecules in an embedded disk does not result in a central depression in emission for highly inclined sources. For the edge-on disk L1527 the central depressions are thus due to a combination of optically thick continuum emission in the central beam, resolved-out line emission, and the subtraction of continuum from optically thick line emission.

A better picture of the spatial origin of the emission can be obtained from position–velocity (PV) diagrams as shown in Figure 1 (middle panels). In principle, in these diagrams, disk emission is located at small angular offsets and high velocities, while envelope emission extends to larger offsets but has lower velocities. The PV diagrams show that the HCO^+ emission peaks at angular offsets of $\sim$1″ and velocities between $\sim$1 and 2 km s^{-1}, while the $H^{13}CO^+$ emission peaks at larger offsets ($\sim$1.″5–3″) and lower velocities ($\lesssim$1 km s^{-1}). The presence of an infalling envelope is also evident from the presence of redshifted emission on the predominantly blueshifted south side of the source and blueshifted emission in the north. These components are strongest for $H^{13}CO^+$. Together, this suggests that the HCO^+ emission is dominated by the disk and innermost envelope and that the $H^{13}CO^+$ emission originates mostly at larger radii ($\gtrsim$140 au). However, if the emission is optically thick, emission observed at small spatial offsets from source center may in fact originate at much larger radii (see, e.g., van 't Hoff et al. 2018b), so the difference between HCO^+ and $H^{13}CO^+$ can be partially due to an optical depth effect.

An absence of HCO^+ inside the water snowline in the inner disk would show up in the PV diagram as an absence of emission at the highest velocities. Because at these highest velocities only emission from the disk, and not from the envelope, is present (see, e.g., Figure A1), this effect can still be visible even if the emission becomes optically thick in the envelope. As a reference, the 3σ contour of $C^{18}O$ $J = 2 - 1$

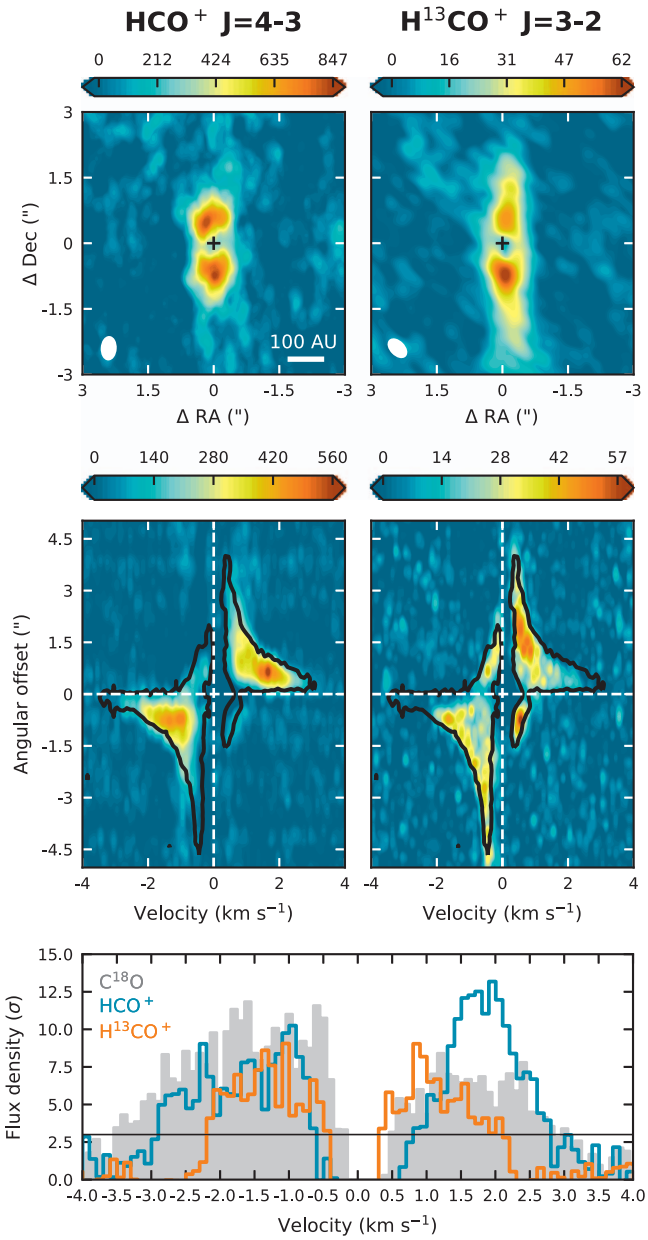

Figure 1. Integrated intensity maps (top) and PV diagrams (middle) for the HCO^+ $J = 4 - 3$ (left) and $H^{13}CO^+$ $J = 3 - 2$ (right) transitions toward L1527. Central velocity channels ($\Delta v \leqslant |0.5|$ km s^{-1}) with resolved-out emission are omitted from the integrated intensity maps. The velocity axis of the PV diagrams is centered on the systemic velocity of 5.9 km s^{-1}, and the $C^{18}O$ $J = 2 - 1$ PV diagram is overlaid in black contours (3σ). The color scale is in mJy beam^{-1} km s^{-1} for the integrated intensity maps and in mJy beam^{-1} for the PV diagrams. The beam is shown in the lower left corner of the top panels, and the velocity resolution is 0.1 km s^{-1}. The bottom panel shows cuts through the PV diagrams close to the midplane (0.″2 and −0.″2 for, respectively, redshifted and blueshifted $C^{18}O$ and HCO^+ emission, and ±0.″5 for $H^{13}CO^+$) to highlight the difference in velocity extent between $C^{18}O$ (solid gray), HCO^+ (blue line), and $H^{13}CO^+$ (orange line). The flux is expressed in factors of σ for each data set, and the horizontal line marks the 3σ level.

emission at comparable resolution (0.″43 × 0.″28) is overlaid on the HCO^+ and $H^{13}CO^+$ PV diagrams. These $C^{18}O$ observations were previously presented by van 't Hoff et al. (2018b), but to maximize the signal-to-noise ratio, we show here the combined data from the long- and short-baseline tracks of the observing program, while van 't Hoff et al. (2018b) only used the long-baseline executions. $C^{18}O$ is present throughout the entire disk, so an absence of HCO^+ and $H^{13}CO^+$ emission at the highest $C^{18}O$ velocities signals a depression or absence of these molecules in the inner region of the disk. The highest blue- and redshifted velocities observed for $C^{18}O$ are −3.6 and +3.0 km s^{-1}, respectively, with respect to the source velocity. HCO^+ reaches velocities close to the highest redshifted $C^{18}O$ velocity, that is, −2.8 and +2.9 km s^{-1}, while $H^{13}CO^+$ is confined between −2.1 and 2.2 km s^{-1} at the 3σ level of the observations (see Figure 1, bottom panel).

A more quantitative constraint on the spatial origin of the emission can be set by considering the velocity structure. To calculate the velocity field, we adopt a Keplerian rotating disk with an outer radius of 125 au (Tobin et al. 2013) embedded in a rotating infalling envelope following the prescription by Ulrich (1976) and Cassen & Moosman (1981). We use a stellar mass of 0.4 $M_\odot$, as this was found to best reproduce ALMA observations of ^{13}CO and $C^{18}O$ (van 't Hoff et al. 2018b). This is slightly lower than the ∼0.45 $M_\odot$ derived by Aso et al. (2017). The resulting midplane velocity field is displayed in Figure A1. For this stellar mass and disk radius, emission at velocities $\gtrsim |2.6|$ km s^{-1} offset from the source velocity originates solely in the disk. The highest-velocity HCO^+ emission observed at the current sensitivity is predominantly coming from the disk at radii $\gtrsim$42 au. All $H^{13}CO^+$ velocity channels contain emission from both disk and envelope. This means that either the observed $H^{13}CO^+$ emission originates solely in the envelope or there is some emission coming from the outer disk (radii $\gtrsim$73 au) as well. As illustrated in Figure A1, these cases are not trivial to distinguish, as the envelope velocity profile results in envelope emission being present at small angular offsets from the protostellar position. However, taken together, these results thus suggest an absence of HCO^+ emission in the inner ∼40 au at the sensitivity of our observations.

4. Modeling of the HCO^+ Emission

To further interpret these observations, we make synthetic HCO^+ and $H^{13}CO^+$ images using the physical structure for L1527 derived by Tobin et al. (2013) and that was also used by van 't Hoff et al. (2018b) and van 't Hoff et al. (2020) to model the ^{13}CO, $C^{18}O$, and $C^{17}O$ emission. In short, this model contains a 125 au Keplerian disk within a rotating infalling envelope (Ulrich 1976; Cassen & Moosman 1981) and is the result of fitting a large grid of 3D radiative transfer models to the thermal dust emission in the (sub)millimeter, the scattered light L' image, and the multiwavelength SED. In order to fit the multiwavelength continuum emission, a parameterized sub/millimeter dust opacity was adopted with a value of 3.5 cm^2 g^{-1} at 850 μm (Andrews & Williams 2005), and the best-fit model has a dust opacity spectral index β of 0.25. This dust opacity suggests that some grain growth has occurred (see Tobin et al. 2013 for more discussion). In our model, the dust then becomes optically thick at radii $\lesssim$4 au for different angular offsets along the disk major axis at the frequency of the HCO^+ $J = 4 - 3$ transition (356.734288 GHz; see Figure A1). The temperature and density structure of the model is shown in Figure A3.

We employ two approaches to constrain the spatial origin of the HCO^+ and $H^{13}CO^+$ emission and the water snowline location. First, we adopt a parameterized abundance structure where the HCO^+ abundance is vertically constant but can change at different radii (Section 4.1). This simple type of

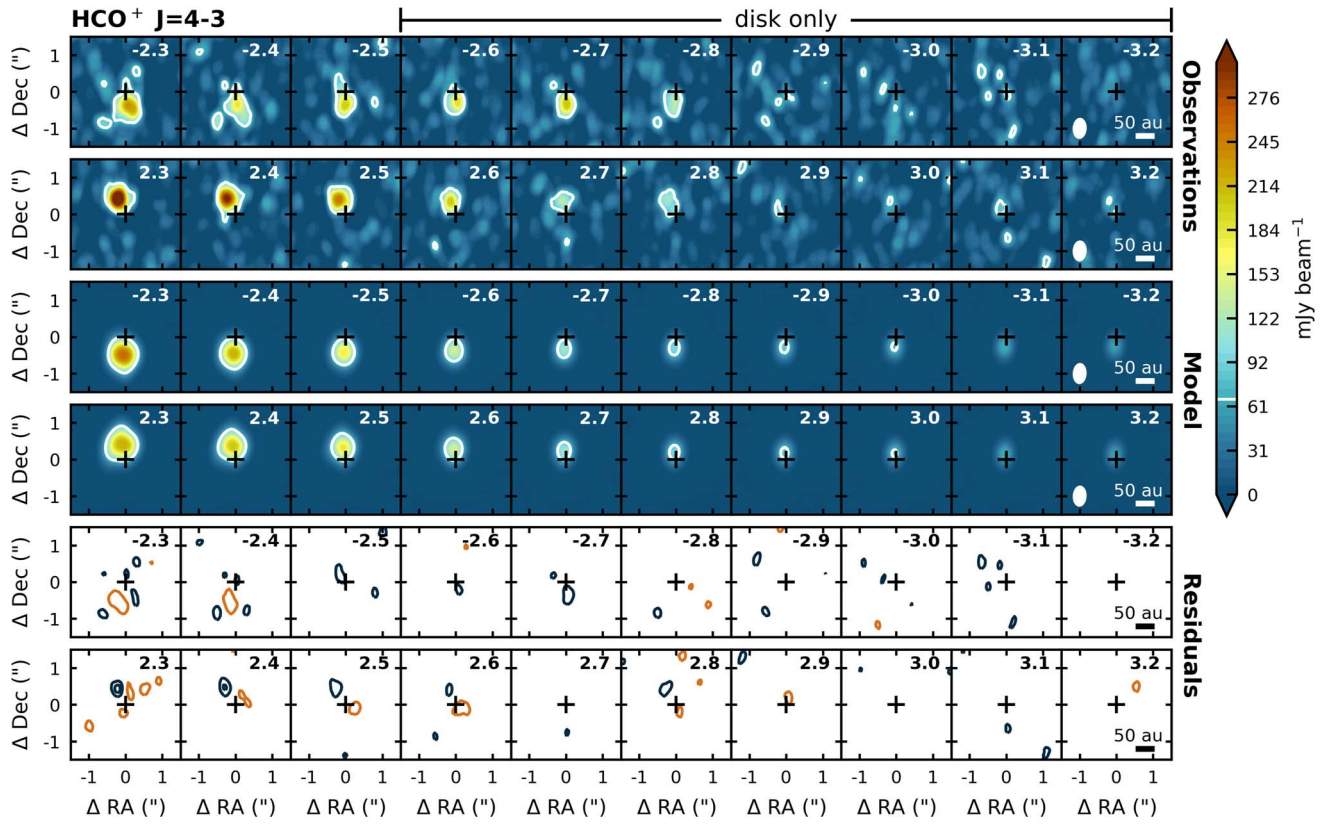

Figure 2. Selected channels of HCO^+ $J = 4 - 3$ emission from observations (top two rows) and from an L1527-specific model with an abundance of 2×10^{-11} at radii $\leqslant$60 au and an abundance of 2×10^{-10} at larger radii (middle two rows). The velocities offset from the source velocity (km s^{-1}) are listed in the upper right corner of each panel, and channels at velocities $\gtrsim |2.6|$ km s^{-1} contain only emission from the disk. A white contour denotes the 3σ level. Residuals after subtracting the model from the observations are shown in the bottom two rows. Black contours are in steps of 3σ starting at 3σ, and orange contours are in steps of -3σ starting at -3σ. The black plus sign marks the continuum peak, and the beam is shown in the lower left corner of the rightmost panels.

model will allow us to address whether the nondetection of HCO^+ and $H^{13}CO^+$ emission at velocities as high as observed for $C^{18}O$ is due to a steep drop in abundance, as expected inside the water snowline. Second, we use a small chemical network for HCO^+ as presented by Leemker et al. (2021) for a more detailed study of the snowline location (Section 4.2). In both cases, image cubes are simulated with the 3D radiative transfer code LIME (Brinch & Hogerheijde 2010), assuming LTE and using molecular data files from the LAMDA database (Schöier et al. 2005; van der Tak et al. 2020). The synthetic image cubes are continuum subtracted and convolved with the observed beam size.

4.1. Parameterized Abundance Structure

Our goal here is to determine whether the absence of HCO^+ and $H^{13}CO^+$ emission in the inner disk is due to a sharp drop in abundance, as expected inside the water snowline. We therefore parameterize the HCO^+ abundance as a function of radius and focus on the intermediate- and high-velocity channels that contain emission from the disk and inner envelope.

Velocity-channel emission maps of a model that reproduces the HCO^+ emission at velocities $\geqslant |2.3|$ km s^{-1} reasonably well are presented in Figure 2. This model has an HCO^+ abundance of 2×10^{-11} at radii $\leqslant$60 au and an abundance of 2×10^{-10} at larger radii. The latter abundance is not high enough to reproduce the observed envelope emission at lower velocities, and this is most likely the reason that the redshifted emission at intermediate velocities (2.3–2.5 km s^{-1}) is slightly underestimated. However, the important result here is that the HCO^+ abundance inside 60 au is low, and therefore the nondetection of emission at velocities $\geqslant |2.9|$ km s^{-1} (tracing the inner $\sim$40 au) could be due to the sensitivity of the observations. Abundances higher than 2×10^{-11} produce emission above the observed 3σ level at velocities $\geqslant |2.9|$ km s^{-1}, but a further drop in abundance at radii $\lesssim$40 au cannot be assessed.

The abundance in the outer disk (>60 au) is hard to constrain as well because the abundances in the outer disk and inner envelope are degenerate. A model with an abundance of 2×10^{-11} throughout the entire disk and an envelope abundance of 1×10^{-9} reproduces the observations equally well as the model displayed in Figure 2. We can break this degeneracy using the $H^{13}CO^+$ observations. As shown in Figure B1, the $H^{13}CO^+$ emission at velocities $\geqslant |1.9|$ km s^{-1} can be reproduced by a model with a constant $H^{13}CO^+$ abundance of 3×10^{-12} in both disk and envelope. For an elemental $^{12}C/^{13}C$ ratio of 68 (Milam et al. 2005), an $H^{13}CO^+$ abundance of 3×10^{-12} suggests an HCO^+ abundance of 2×10^{-10}. Together, these modeling results thus suggest that the HCO^+ abundance is lower in the disk than in the envelope, with abundances of 2×10^{-10} in the outer disk (>60 au), 2×10^{-11} at 40–60 au, and $\leqslant 2 \times 10^{-11}$ at radii <40 au.

Jørgensen et al. (2004) derived an $H^{13}CO^+$ abundance of 8.5×10^{-12} for the envelope around L1527 from multiple single-dish observations. This is within a factor of three of our derived abundance of 3×10^{-12}, and consistent with our result

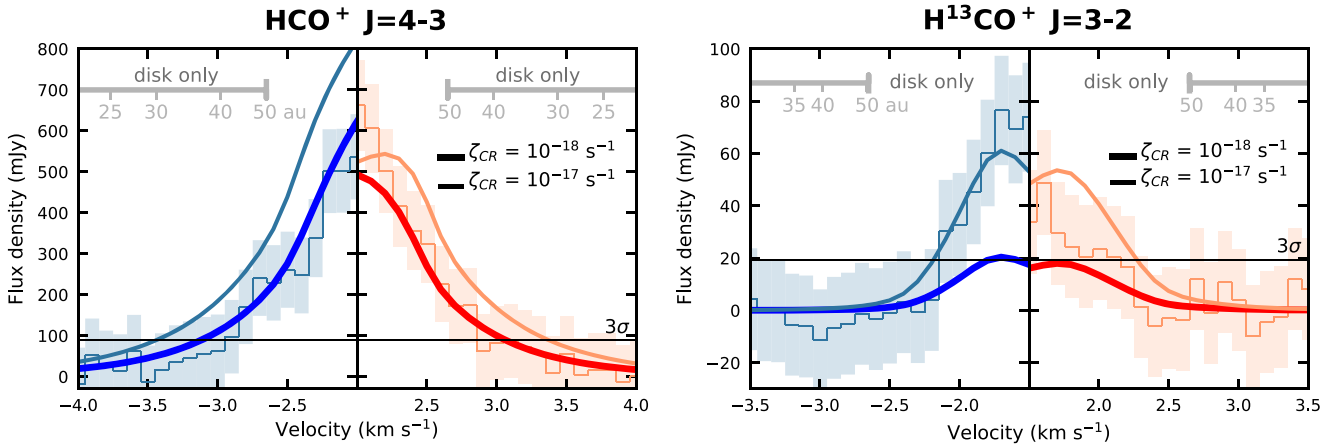

Figure 3. Spectra of the HCO^+ (left panel) and $H^{13}CO^+$ (right panel) emission extracted in a 0.″75 aperture centered on the blueshifted emission peak (left sides of each panel) and on the redshifted emission peak (right sides of each panel). The observations are displayed in discrete velocity bins of 0.1 km s^{-1}, with the shaded area depicting the 3σ uncertainty and a 10% flux calibration uncertainty. The smooth lines are for models with a CO abundance of 10^{-4} and an H_2O abundance of 10^{-6}, but with varying CR ionization rates of 10^{-18} s^{-1} (thick line; referred to as the fiducial model) and 10^{-17} s^{-1} (thin line; canonical CR ionization rate). The horizontal black line marks the 3σ level. The velocity range containing only emission from the disk is marked by gray bars in the top of the panels, and the maximum radius probed at certain velocities is indicated. The displayed velocity range is different for both molecules.

that the abundance increases at larger radii. Our derived HCO^+ abundances on disk scales are consistent with the modeling results from Leemker et al. (2021) for protoplanetary disks around Herbig stars, which show a similar HCO^+ abundance gradient in the outer disk (20–100 au) and a stronger decrease across the snowline (4.5 au) with the abundance dropping below 10^{-12}. The current observations are not sensitive enough to constrain such low abundances. However, since the HCO^+ abundance also depends on density and ionization, chemical modeling using a physical model specific for L1527 is required to link the abundance structure to the snowline.

4.2. Chemical Modeling

The chemical network presented by Leemker et al. (2021) was developed to study the relationship between the water snowline and HCO^+ (and $H^{13}CO^+$) emission in Herbig disks. It contains the main formation and destruction reactions for HCO^+, as well as the freezeout and thermal desorption of water, as illustrated in Figure C1. Reaction rate constants are taken from the UMIST database (McElroy et al. 2013) and are listed in Table 2 of Leemker et al. (2021). For water, a binding energy of 5775 K is used, which corresponds to an amorphous water ice (Fraser et al. 2001).

Freezeout of CO, the parent gas-phase molecule of HCO^+, was not included in the study by Leemker et al. (2021), as this only occurred in the low-density outer region of the Herbig disks. Although there is no sign of CO freezeout in the disk around L1527 (van 't Hoff et al. 2018b, 2020), we have added the freezeout and thermal desorption of CO to the chemical network for completeness and to display the HCO^+ abundance structure in the envelope. The exact temperature at which CO desorbs depends on the composition of the ice (e.g., Collings et al. 2003), with pure CO ice desorbing at lower temperatures (855 K; Bisschop et al. 2006) than CO ice on top of water ice (1150 K; Garrod & Herbst 2006). The resulting desorption temperatures differ by ∼6 K; for example, 18 K versus 24 K for a density of 10^7 cm^{-3}. In either case the CO snowline is located outside the L1527 disk, at ∼500 au or ∼200 au, respectively, and we adopt the binding energy of 855 K for a pure CO ice (Bisschop et al. 2006). Including or excluding freezeout of CO does not influence the HCO^+ emission in the disk and inner envelope velocity channels that we are interested in here.

The freezeout rates depend on the available surface area of the dust grains. Following Leemker et al. (2021), we assume a typical grain number density of $10^{12} \times n(H_2)$ and a grain size of 0.1 μm. Even if a fraction of the grains have grown to larger sizes, the smallest grains will dominate the surface area, and van 't Hoff et al. (2017) showed that adopting a more detailed description for the available surface area did not significantly affect the predicted N_2H^+ abundance for the protoplanetary disk around TW Hya. For the radiative transfer, we use the dust opacities from Tobin et al. (2013) as described at the beginning of Section 4.

Initially, all abundances are set to zero, except for H_2, gas-phase CO and gas-phase H_2O, and we run the chemistry for 10^5 yr. Running the chemistry for 10^6 yr, as typically done for protoplanetary disk studies, does not affect the HCO^+ abundance structure in the disk and inner envelope (radii $\lesssim$1000 au; see Appendix C). The main free parameters in the model are the initial CO and H_2O abundance and the CR ionization rate, which initiates the ion-neutral chemistry by ionizing H_2. The model does not include isotope-specific reactions, and we adopt a $^{12}C/^{13}C$ ratio of 68 (Milam et al. 2005) to generate $H^{13}CO^+$ image cubes.

Van 't Hoff et al. (2018b) did not find evidence for a CO abundance much lower than the canonical value of 10^{-4} in the L1527 disk, and Harsono et al. (2020) derived an upper limit for the H_2O abundance of 10^{-6}. A model with these initial abundances reproduces the HCO^+ and $H^{13}CO^+$ observations equally well as the parameterized model described in Section 4.1. For HCO^+ a CR ionization rate of 10^{-18} s^{-1} (about one order of magnitude below the canonical value) needs to be adopted (see Figure 3). The asymmetry between blueshifted and redshifted emission is due to the kinematics of the disk and envelope, with the envelope in front of the disk for redshifted emission and the envelope behind the disk for blueshifted emission (see Appendix C). Since the HCO^+ observations are more sensitive to the disk than the $H^{13}CO^+$ observations, as discussed in Sections 2 and 4.1, we will focus first on the model that reproduces the HCO^+ emission, and we will discuss the ionization rate in more detail in Section 5.2.

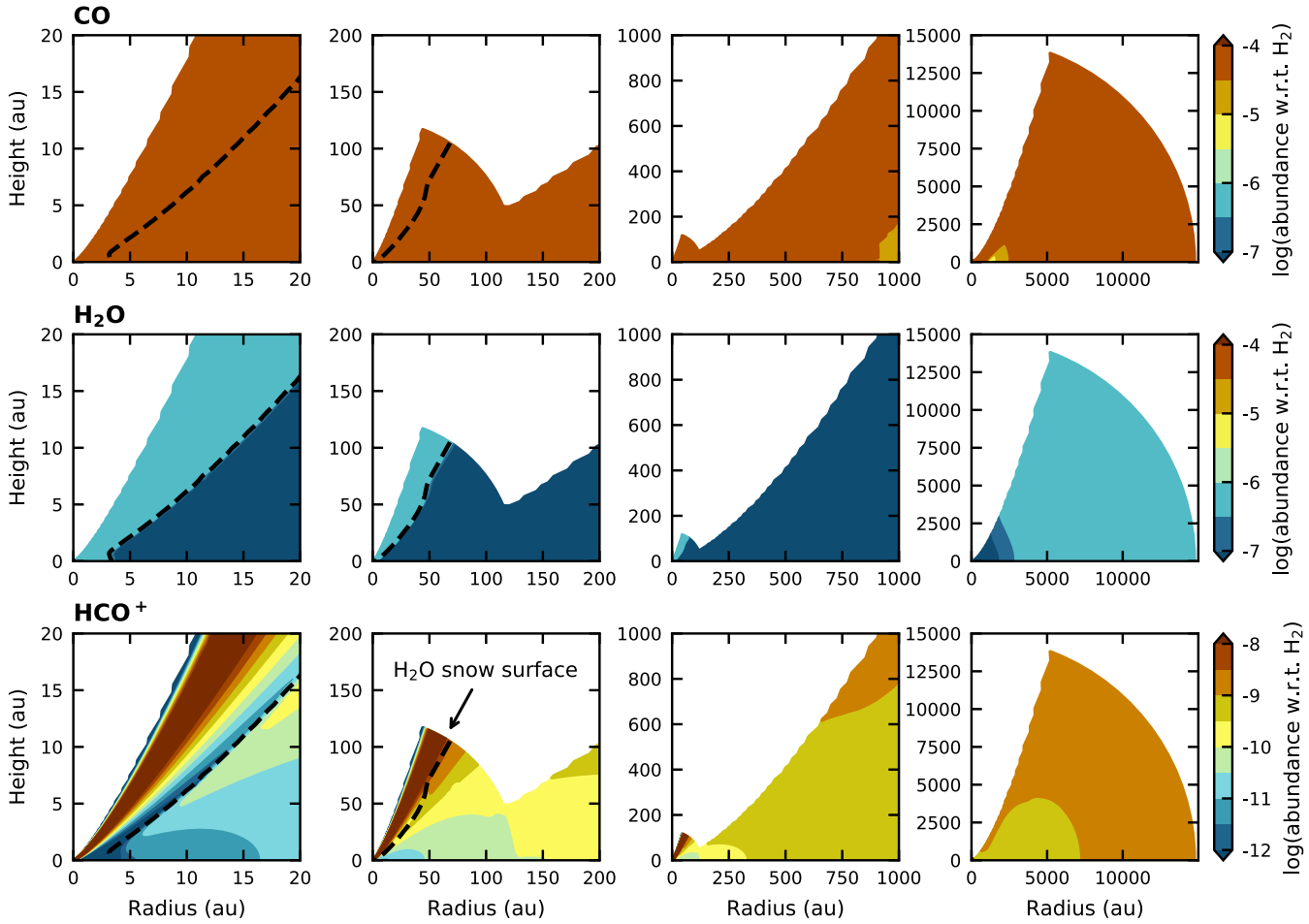

Figure 4. Abundance structure for CO (top panels), H_2O (middle panels), and HCO^+ (bottom panels) predicted by the fiducial chemical model with initial CO and H_2O abundances of 10^{-4} and 10^{-6}, respectively, and a CR ionization rate of 10^{-18} s^{-1} for the physical structure of L1527. From left to right, panels display larger spatial scales. The disk outer radius is 125 au. The dashed line in the two leftmost columns marks the H_2O snow surface and the midplane snowline at 3.4 au.

The abundance structure reproducing the HCO^+ observations (our fiducial model with $X(CO) = 10^{-4}$, $X(H_2O) = 10^{-6}$, and $\zeta_{CR} = 10^{-18}$ s^{-1}) is presented in Figure 4. For the adopted temperature and density structure, the water snowline is located at 3.4 au, which corresponds to a temperature of 140 K. The snow surface is located high up in the disk surface layers, making most of the disk and the inner envelope devoid of gas-phase water. Water is present in the gas phase at radii $\gtrsim$3000 au because the density in the outer envelope becomes too low for water to freeze out in the timescale of the model. A similar water abundance profile was found by Schmalzl et al. (2014), who used a simplified chemical network that was benchmarked against three full chemical networks to model Herschel observations of water in protostellar envelopes.

Overall, the HCO^+ abundance gradually decreases with increasing density and steeply decreases across the water snow surface. At the high midplane densities, the HCO^+ abundance remains low directly outside the water snowline as shown in earlier work (van 't Hoff et al. 2018a; Hsieh et al. 2019). In the midplane, the HCO^+ abundance drops from 10^{-11} at 16 au to 3×10^{-12} at 5 au and then steeply drops to abundances $<10^{-12}$ inside the snowline. These abundances are all at least an order of magnitude lower than the upper limit derived for the high-velocity channels probing radii $\leqslant$40 au using the parameterized model in Section 4.1. The sensitivity of the observations is thus not high enough to probe the HCO^+ abundance drop across the snowline, and the absence of emission in the highest-velocity channels cannot be linked to the snowline. The high HCO^+ abundance in the uppermost surface layers of the disk is likely because CO photodissociation is not included in the model. In this region, the rate for the reaction between HCO^+ and H_2O,

$$R_{\rm destruction} \propto n(HCO^+)n(H_2O), \quad (1)$$

is low because the low density results in a low H_2O number density, $n(H_2O)$. As discussed by Leemker et al. (2021), electron recombination becomes the dominant destruction mechanism of HCO^+ in this region. At the same time, the HCO^+ formation rate,

$$R_{\rm formation} \propto n(CO)n(H_3^+), \quad (2)$$

remains high, as the H_3^+ number density is set by the CR ionization rate and is therefore independent of density. Including CO photodissociation would remove the parent molecule CO and hence prevent HCO^+ formation, but knowledge of the UV field is required for a proper implementation. However, this low-density layer does not significantly contribute to the total HCO^+ emission. Manually removing this layer before radiative transfer results in flux differences less than 0.2% and spectra identical to those displayed in Figure 3.

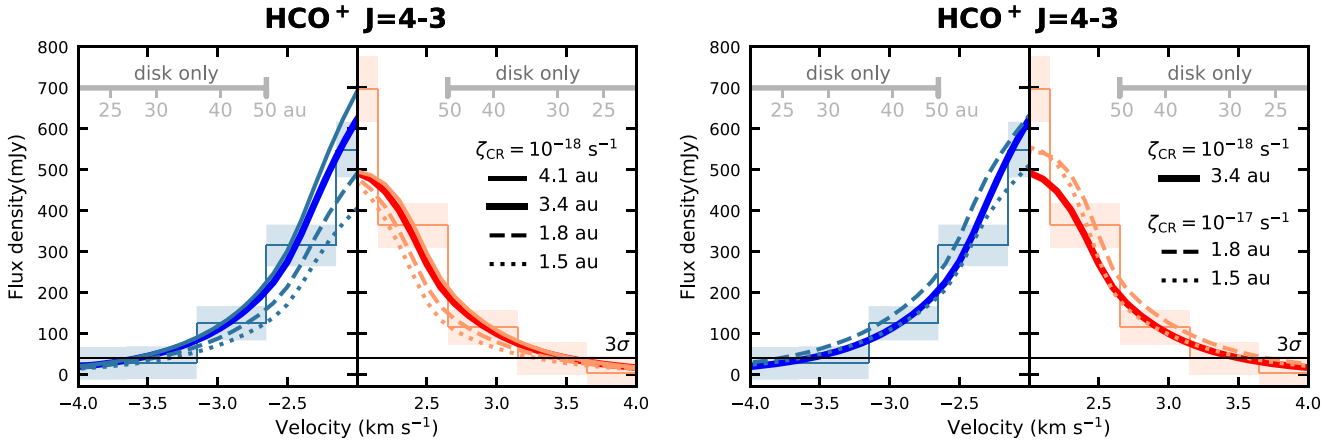

Figure 5. Spectra of the HCO^+ emission extracted in a 0.″75 aperture centered on the blueshifted emission peak (left side of each panel) and on the redshifted emission peak (right side of each panel). The observations are binned to 0.5 km s^{-1}, and the shaded area depicts the 3σ uncertainty and a 10% flux calibration uncertainty. The thick dark colored lines are for the fiducial model with a snowline at 3.4 au. The other lines represent models where the disk temperature has been multiplied by a constant factor to obtain snowline locations of 1.5 au (dotted line), 1.8 au (dashed line), and 4.1 au (thin solid line). The CR ionization rate is 10^{-18} s^{-1} for the models in the left panel and 10^{-17} s^{-1} in for the models in the right panel, except for the fiducial model (thick line), which is the same as in the left panel. The horizontal black line marks the 3σ level. The velocity range containing only emission from the disk is marked by gray bars in the top of the panels, and the maximum radius probed at certain velocities is indicated.

The HCO^+ abundance is barely influenced by CO freezeout because this occurs only in a small region of the envelope. In the disk and inner envelope ($\lesssim$900 au), the temperature is too high for CO to freeze out, while at radii $\gtrsim$2500 au the density becomes too low for CO to freeze out within 10^5 yr, resulting in CO being present in the gas phase at the initial abundance throughout the majority of the system. A similar abundance profile was derived by Jørgensen et al. (2005) for a sample of 16 sources, and ^{13}CO has been observed out to radii of ~10,000 au toward L1527 (Zhou et al. 1996). Running the chemistry for 10^6 yr results in a midplane region with a decreased HCO^+ abundance centered around 2500 au due to higher levels of CO freezeout. Simultaneously, the higher levels of H_2O freezeout increase the HCO^+ abundance, resulting overall in only a small region with a lower HCO^+ abundance at radii $\gtrsim$1000 au after 10^6 yr. The HCO^+ abundance at smaller radii is unaffected (see Figure C2).

The HCO^+ abundance structure in the disk as presented in Figure 4 is very robust with respect to changes in the initial CO and H_2O abundance. Aso et al. (2017) suggested a CO abundance of 2×10^{-5} based on ALMA observations of C^{18}O, but lowering the CO abundance two orders of magnitude does not affect the HCO^+ abundance in the disk significantly (see Figure C3). The only changes are a lower HCO^+ abundance in the uppermost surface layers of the disk (above the snow surface) and a lower abundance at radii $\gtrsim$900 au. A canonical H_2O abundance of 10^{-4} increases the vertical height of the HCO^+ depleted layer above the snow surface and strongly decreases the HCO^+ abundance at radii $\gtrsim$1500 au (see Figure C4). Lowering the H_2O abundance further to 10^{-7} slightly increases the HCO^+ abundance above the snow surface. The HCO^+ abundance thus remains unaltered throughout the majority of the disk for CO abundances between 10^{-4} and 10^{-6} and H_2O abundances between 10^{-4} and 10^{-7}.

The only parameter that has a strong impact on the HCO^+ abundance in the disk is the CR ionization rate. As described in van 't Hoff et al. (2018a), the HCO^+ abundance is proportional to the square root of the CR ionization rate. Hence, a canonical value of 10^{-17} s^{-1} results in an HCO^+ abundance higher by a factor ~3 compared to a rate of 10^{-18} s^{-1} (Figure C5 vs. Figure 4) and a too high HCO^+ flux compared to what is observed (see Figure 3). The predicted HCO^+ flux for a CR ionization rate of 10^{-17} s^{-1} is less than a factor of 3 higher than the flux predicted for a rate of 10^{-18} s^{-1}, signaling that the emission becomes optically thick.

5. Discussion

5.1. The Water Snowline Location in L1527

For the temperature and density structure derived by Tobin et al. (2013), the water snowline is predicted to be at 3.4 au in the disk around L1527, and the corresponding HCO^+ abundance structure from a small chemical network calculation can reproduce the observed HCO^+ emission. Although the current observations are not sensitive to the expected HCO^+ abundance changes across the snowline, the chemical model shows a decrease in the HCO^+ abundance over a much larger radial range above the snow surface. This suggests that the snowline location may be constrained indirectly from HCO^+ emission based on the global temperature structure. To investigate the stringency of the current observations, we run a set of models with different snowline locations separated by ~0.2–0.5 au generated by multiplying the fiducial temperature structure in the disk by a constant factor. To obtain the maximum sensitivity, we bin the observations to 0.5 km s^{-1}.

Figure 5 displays the HCO^+ spectra for models with a snowline at 1.5, 1.8, 3.4 (fiducial), and 4.1 au. The differences between these models are too small to be distinguished at disk-only velocities, but the current sensitivity is high enough to see a significant difference at a $\pm$2.4 km s^{-1} velocity offset. While a snowline at 1.8 au produces HCO^+ emission at about the 3σ uncertainty level (including a 10% flux calibration uncertainty), a snowline at 1.5 au clearly underproduces the emission. The effect of a warmer disk is not very pronounced at redshifted velocities, but a snowline at 4.1 au slightly overproduces the blueshifted emission. Lower HCO^+ emission as a result of a colder disk can partially be compensated by a higher CR ionization rate. For $\zeta_{CR} = 10^{-17}$ s^{-1}, a snowline at 1.5 au can reproduce the observed HCO^+ emission, while a snowline at 1.8 au results in a too high flux. However, van 't Hoff et al.

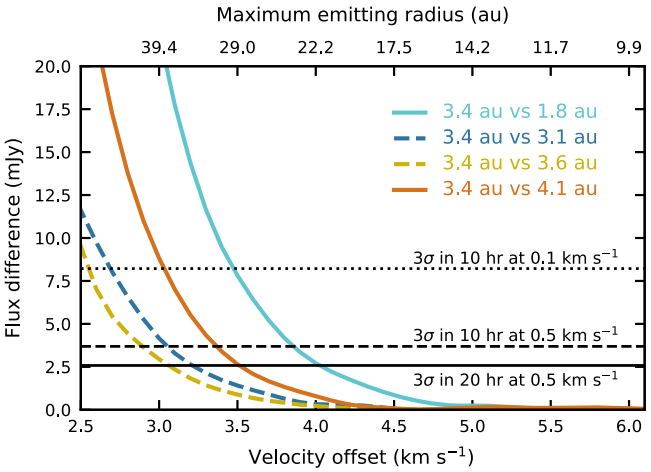

Figure 6. Difference in HCO^+ $J = 4 - 3$ flux between models with different snowline locations and the fiducial model with the snowline at 3.4 au at velocity offsets that trace only the disk. The top horizontal axis shows the maximum radius probed at a certain velocity for an edge-on Keplerian disk around a 0.4 $M_\odot$ star as used for L1527. The dotted and dashed lines mark the 3σ limit that can be reached with ALMA in 10 hr on source at a spectral resolution of 0.1 and 0.5 km s^{-1}, respectively. The solid line is the 3σ limit at 0.5 km s^{-1} for 20 hr on source. The 3σ sensitivity of the current HCO^+ observations is 40 mJy at 0.5 km s^{-1}.

(2018b) were not able to reproduce the ^{13}CO and $C^{18}O$ $J = 2 - 1$ emission with the temperature structure corresponding to a 1.5 au snowline (their Intermediate Model), instead requiring a warmer disk. Changing the temperature also in the envelope has only a small effect on the emission at $\pm$ 2.4 km s^{-1} (Figure A2). Taken together, for the here-adopted physical structure, these results thus suggest a snowline radius of 1.8–4.1 au if $\zeta_{CR} = 10^{-18}$ s^{-1} and between 1.5 and 1.8 au for $\zeta_{CR} = 10^{-17}$ s^{-1}.

No other molecular line observations are currently available to locate the water snowline in L1527: $H_2^{18}O$ emission has not been detected (Harsono et al. 2020), and while weak methanol emission has been observed, the sensitivity and resolution of those data were insufficient to determine its spatial origin (Sakai et al. 2014). Aso et al. (2017) presented a warmer model based on fitting of submillimeter continuum visibilities than the model derived by Tobin et al. (2013) and used in this work, with the snowline at ~8 au. This is at least twice as far out as predicted here based on the HCO^+ models, but the temperature profile is kept fixed in the fitting procedure of Aso et al. (2017). Van 't Hoff et al. (2018b) inferred a temperature profile based on optically thick ^{13}CO and $C^{18}O$ emission, which has a temperature of ~35 K at 40 au. The temperature in the inner ~20 au depends strongly on the chosen power-law coefficient and does not provide a strong constraint on the snowline location.

Providing stronger constraints on the snowline location using HCO^+ emission will require significantly deeper observations as illustrated in Figure 6. As higher velocities trace emission originating out to smaller radii, the total flux decreases at higher velocities, and hence higher sensitivity is required to distinguish two models. Ideally, one would want to compare the flux in a certain velocity channel with the flux of models with the snowline inside and outside the maximum radius probed by that velocity. However, it is immediately clear from Figure 6 that this is not possible for L1527 with current facilities, as flux differences at $\gtrsim |4.0|$ km s^{-1} (corresponding to a ~20 au radius) become too small to be observed in 20 hr on source with ALMA.

Nonetheless, deeper integrations will allow for better constraints in two ways. First, a higher sensitivity will allow different models to be compared over more velocity channels, and in particular, in channels that only trace disk emission. This will remove any influence from the envelope. For example, 10 hr on source with ALMA will result in 5–10 0.1 km s^{-1} disk-only channels (or two to three channels at 0.5 km s^{-1}) where models with snowlines at 1.8, 3.4, and 4.1 au can be distinguished, as compared to currently one 0.5 km s^{-1} channel containing emission from both disk and envelope. Second, a higher sensitivity will allow us to distinguish between models with smaller differences in snowline radius. With 10 hr on source, the snowline can be constrained within a few tenths of an au, although there will be a degeneracy with the CR ionization rate.

Higher-J transitions will generally trace warmer and denser material, but, in turn, higher dust opacity at higher frequencies may prevent us from observing these transitions from the inner disk. For the here-adopted dust opacities, the continuum $\tau = 1$ surface shifts outward by only ~1 au for the $J = 8 - 7$ transition (713.342090 GHz) compared to the $J = 4 - 3$ transition (356.734288 GHz; Figure A1), suggesting that the dust opacity is not a strong limiting factor in choosing an HCO^+ transition. For proper treatment of higher-J transitions, UV heating of the gas has to be taken into account, and this emission may arise from a thin layer in which the gas and dust temperatures are decoupled (e.g., Visser et al. 2012). Such a modeling approach was adopted by Leemker et al. (2021), while we here adapt the dust temperature structure for L1527 and assume that the gas and dust temperature are equal, which is appropriate for the $J = 4 - 3$ transition, which emits from regions where the temperatures are coupled (e.g., Mathews et al. 2013).

That being said, in our model the integrated flux at high velocities ($\gtrsim |3|$ km s^{-1}) increases up to a factor of ~2 or ~3 for the $J = 5 - 4$ (445.902996 GHz) and $J = 7 - 6$ (624.208673 GHz) transitions, respectively, compared to the $J = 4 - 3$ flux in the fiducial model (not shown). The flux of the $J = 8 - 7$ transition is similar to the $J = 7 - 6$ flux at velocities originating solely in the disk. For the $J = 7 - 6$ transition, the curves in Figure 6 shift to the right by ~1 km s^{-1}, suggesting that it is easier to distinguish between different snowline locations. However, the decrease in atmospheric transmission results in significantly lower sensitivities that make high-sensitivity observations very expensive: in 20 hr on source at 0.5 km s^{-1} resolution, an rms of 224, 25, and 20 mJy is reached for $J = 5 - 4$, $J = 7 - 6$, and $J = 8 - 7$, respectively. These sensitivities would just be enough to distinguish between a snowline at 1.8, 3.4, or 4.1 au at velocity offsets <3 km s^{-1} with the $J = 7 - 6$ and $J = 8 - 7$ transitions. As even for the $J = 1 - 0$ (89.188523 GHz) transition the snowline coincides with the dust $\tau = 1$ surface, the HCO^+ $J = 4 - 3$ transition is the best suited to constrain the snowline location.

With such long integration times required to derive stronger constraints on the snowline location from HCO^+ emission, it is worth investigating whether the snowline can be located directly with water observations. As shown in Figure A1, the snowline is expected to be hidden behind optically thick dust for frequencies above ~90 GHz, so a direct detection of the

snowline would not be possible for L1527. However, locating the snowline directly with water observations may still turn out to be a viable route for sources that have the water snowline extend beyond the radius where the dust becomes optically thick.

5.2. Cosmic-Ray Ionization Rate

Another important result concerns the CR ionization rate in the disk of L1527. The CR ionization rate is crucial for both the physical and chemical evolution of the disk. From a physical perspective, ionization plays an important role in angular momentum transport through the magnetorotational instability (MRI; e.g., Balbus & Hawley 1991). From a chemical point of view CRs are the driver of chemistry in the disk midplane, where other ionizing agents cannot penetrate (e.g., Eistrup et al. 2016, 2018). For the here-adopted physical structure of L1527 that is able to reproduce multiwavelength continuum emission (Tobin et al. 2013) and CO isotopologue emission (van 't Hoff et al. 2018b), a canonical CR ionization rate of 10^{-17} s^{-1} overproduces the HCO^+ emission, which originates predominantly from radii $\gtrsim$40 au (Figure 3). The $H^{13}CO^+$ emission, which is originating predominantly from the inner envelope, does require a CR ionization rate of 10^{-17} s^{-1} (Figure 3).

In order to reproduce the HCO^+ observations with a CR ionization rate of 10^{-17} s^{-1}, the disk temperature needs to be lowered such that the snowline is located inside of 1.8 au (instead of 3.4 au; Figure 5). A temperature structure obtained by multiplying our fiducial temperature by a constant factor of 0.6, resulting in a snowline at 1.5 au, is too cold to explain the ^{13}CO and $C^{18}O$ $J = 2 - 1$ emission (van 't Hoff et al. 2018b), but the CO isotopologue observations are not sensitive enough to confidently say whether the temperature structure associated with a 1.8 au snowline is too cold as well. We have assumed that the temperature changes globally by a constant factor, and this analysis cannot rule out that a model with a slightly flatter temperature profile (i.e., colder in the inner few au) would be able to explain the molecular line observations with a canonical CR ionization rate. Higher-sensitivity observations of CO isotopologues or other temperature tracers are required to better constrain the detailed temperature structure.

A snowline location different from 3.4 au could be obtained by, for example, a different luminosity or different disk mass. Measurements of the bolometric luminosity based on the spectral energy distribution (SED) range between 1.6 and 2.0 $L_\odot$ (Tobin et al. 2008; Green et al. 2013; Karska et al. 2018). This is likely an underestimation of the true luminosity, as edge-on sources embedded in an envelope can have internal luminosities up to ~2 times higher than the bolometric luminosity (Whitney et al. 2003). For a 1 $L_\odot$ protostar, Tobin et al. (2008) require an accretion luminosity of 1.6 $L_\odot$ to fit the SED, resulting in a true bolometric luminosity of ~2.6 $L_\odot$. The model used here has a total luminosity of 2.75 $L_\odot$ (Tobin et al. 2013), and assuming that the snowline radius scales as the square root of the luminosity, a luminosity of 0.8 $L_\odot$ would be required for a snowline radius of 1.8 au. This is a factor of two smaller than derived from the SED. A lower disk mass could also shift the snowline inward, but for an accretion rate of 3×10^{-7} $M_\odot$ yr^{-1} (corresponding to an accretion luminosity of 1.6 $L_\odot$), models by Harsono et al. (2015) show less than 1 au difference between disk masses of 0.05 and 0.1 $M_\odot$. The disk mass of the model used here is 0.0075 $M_\odot$. Modeling of high-resolution ALMA data, for example, from the FAUST or eDisk large programs may provide additional constraints on the disk structure.

Chemically, a canonical CR ionization rate may be reconciled with the observations if there is a higher destruction rate of HCO^+. In our model, HCO^+ can be destroyed by H_2O and electrons, where the electrons are provided by ionization of H_2 by CRs. Since grains are likely negatively charged (Umebayashi & Nakano 1980), ions may also recombine on dust grains. The recombination rate for this process, $R_{\rm grain}$, is given by

$$R_{\rm grain} = a_g n_{\rm H} n({\rm HCO^+}), \quad (3)$$

where a_g is the recombination rate coefficient ($a_g \approx 10^{-17}$ cm^3 s^{-1}; Umebayashi & Nakano 1980) and $n_{\rm H}$ and $n(HCO^+)$ are the hydrogen and HCO^+ number density, respectively. The recombination rate in the gas phase, $R_{\rm gas}$, is given by

$$R_{\rm gas} = k n_e n({\rm HCO^+}), \quad (4)$$

where n_e is the electron density. The reaction rate coefficient, k, has a temperature dependence and is (4–8) $\times 10^{-7}$ cm^3 s^{-1} for temperatures between 150 and 50 K (UMIST database; McElroy et al. 2013). This means that the grain recombination rate becomes larger than the gas-phase recombination rate for electron abundances, $n_e/n_{\rm H}$, $\gtrsim 10^{-11}$. Since the electron abundance is approximately equal to the HCO^+ abundance, this condition is only met in the disk midplane inside ~16 au for the fiducial model (Figure 4) and only inside ~5 au for the model with a CR ionization rate of 10^{-17} s^{-1} (Figure C5). Destruction of HCO^+ via electron recombination on grains is thus unlikely to affect the predicted HCO^+ abundance.

While we cannot fully rule out a canonical CR ionization rate, the different ionization rates derived from HCO^+ and $H^{13}CO^+$ are not necessarily in conflict with each other. The lower-J transition and lower velocities probed with $H^{13}CO^+$ make the $H^{13}CO^+$ observations more sensitive to the inner envelope than the HCO^+ observations. This would then suggest that the CR ionization rate is lower in the disk compared to the envelope, which could simply be the result of stronger attenuation of external CRs due to the higher density of the disk. The CR ionization rate is expected to decrease exponentially with an attenuation column of 96 g cm^{-2} (Umebayashi & Nakano 1981, 2009) or even higher (Padovani et al. 2018). However, a column larger than 96 g cm^{-2} is only reached in the inner 0.5 au in our L1527 model. Another explanation for a low CR ionization rate in the disk may be the exclusion of CRs by stellar winds and/or magnetic fields as proposed by Cleeves et al. (2015) for the protoplanetary disk around TW Hya. The same mechanism could explain the gradient in CR ionization rate derived for the IM Lup disk, where the steep increase in CR ionization rate in the outer disk may indicate the boundary of the "T Tauriosphere," that is, a stellar-wind-induced boundary analogous to the Sun's heliosphere (Seifert et al. 2021).

While models show that CRs can be produced by jet shocks and by accretion shocks at protostellar surfaces (Padovani et al. 2015, 2016), the transport of CRs in protostellar disks is very complicated (as shown for external CRs by Padovani et al. 2018). Models by Gaches & Offner (2018) for the simpler case of protostellar cores show a difference of five orders of magnitude in CR ionization rate between the two limiting cases of transport of internally created CRs through the core.

In our chemical network, all ionization is provided by CRs, but UV and X-ray ionization can play a role as well, in particular in higher layers in the disk with X-rays penetrating deeper than UV radiation (see, e.g., Cleeves et al. 2014; Notsu et al. 2021; Seifert et al. 2021). However, it is not clear at what point during stellar evolution the dynamo turns on and X-rays are emitted, and no X-ray emission has been detected toward L1527 with Chandra (Güdel et al. 2007). Since the observations constrain the HCO^+ abundance, a significant contribution of UV and/or X-rays to the HCO^+ chemistry would mean that the CR ionization rate is even lower than $10^{-18}\,s^{-1}$.

Other observational constraints for the CR ionization rate in the L1527 disk do not currently exist. Favre et al. (2017) used Herschel observations of the ratio between HCO^+ $J=6-5$ and N_2H^+ $J=6-5$ to constrain the ionization rate in Class 0 protostars, but the upper limit resulting from the nondetection of N_2H^+ toward L1527 only constrains the CR ionization rate to be smaller than $10^{-14}\,s^{-1}$. The signal-to-noise ratio of the $J=6-5$ observations is too low to detect emission at velocity offsets $\gtrsim 2\,km\,s^{-1}$, so they do not help in constraining the HCO^+ distribution or disk temperature structure.

If confirmed, a low CR ionization rate in a young disk may have profound consequences, as high ionization levels are crucial for disk evolution. For example, for angular momentum transport through MRI, the gas needs to be coupled to the magnetic field (Gammie 1996), and hence insufficient ionization may suppress MRI and create a low-turbulence "dead zone," favorable for planetesimal formation (e.g., Gressel et al. 2012). From a chemical perspective, the up-to-two-order-of-magnitude CO depletion observed in protoplanetary disks can only be reproduced by models with CR ionization rates on the order of $10^{-17}\,s^{-1}$ (Bosman et al. 2018; Schwarz et al. 2019). Currently, the CO snowline is located outside the L1527 disk (van 't Hoff et al. 2018b), but unless the CR ionization rate would increase at later stages, a CR ionization rate of $10^{-18}\,s^{-1}$ would suggest that no chemical processing of CO will occur in the L1527 disk once the disk has cooled enough for the CO snowline to shift inward.

6. Conclusions

We have presented $\sim 0\farcs5$ ($\sim$70 au) resolution ALMA observations of HCO^+ $J=4-3$ and $H^{13}CO^+$ $J=3-2$ toward the embedded disk L1527. In order to constrain, for the first time, the water snowline location in a young disk, we modeled the HCO^+ abundance and emission using a physical model specific for L1527 (Tobin et al. 2013) and a small chemical network (based on Leemker et al. 2021). Our main results are summarized below.

1. The observed HCO^+ emission traces the disk down to a radius of $\sim$40 au. The emission can be reproduced with the L1527-specific physical structure that has the water snowline at 3.4 au, given that the CR ionization rate is lowered to $10^{-18}\,s^{-1}$.
2. Even though the observations are not sensitive to the expected HCO^+ abundance change across the midplane snowline, the change across the radial snow surface and the global temperature structure allow us to constrain the snowline location between 1.8 and 4.1 au by multiplying the fiducial temperature structure by a constant factor. The snowline can be inward of 1.8 au if the CR ionization rate is $10^{-17}\,s^{-1}$, but a previous analysis showed that a temperature structure with the snowline at 1.5 au is too cold to reproduce the ^{13}CO and $C^{18}O$ observations.
3. The HCO^+ abundance structure in the disk predicted by the small chemical network is very robust for the initial H_2O and CO abundance and only significantly depends on the CR ionization rate.
4. The observed $H^{13}CO^+$ emission extends out to lower velocity offsets than the HCO^+ emission, indicating that the emission predominantly originates in the inner envelope. For the adopted physical structure, a canonical CR ionization rate of $10^{-17}\,s^{-1}$ is required to reproduce the $H^{13}CO^+$ emission. Together, the HCO^+ and $H^{13}CO^+$ results suggest that the CR ionization rate has a canonical value of $10^{-17}\,s^{-1}$ in the inner envelope and may be attenuated to $\sim 10^{-18}\,s^{-1}$ in the disk.

These results demonstrate the use of HCO^+ as a snowline tracer in embedded disks. However, as long integration times with ALMA are required to detect emission at high velocities to eliminate envelope contribution and to constrain the snowline to within 0.5 au, the direct detection of the snowline through observations of water isotopologues may still prove to be a viable strategy. Deep water observations of a range of different sources are required to constrain when water observations are viable and when we have to resort to indirect tracing with HCO^+. Observations of water ice with the James Webb Space Telescope may provide constraints on the (vertical) snowline as well. In sources with a direct measurement of the snowline location, HCO^+ observations will allow us to constrain the CR ionization rate.

We would like to thank the referee, Ewine van Dishoeck, Martijn van Gelder, and Naomi Hirano for feedback on the manuscript. This paper makes use of the following ALMA data: ADS/JAO.ALMA#2012.1.00193.S and ADS/JAO.ALMA#2012.1.00346.S. ALMA is a partnership of ESO (representing its member states), NSF (USA) and NINS (Japan), together with NRC (Canada), MOST and ASIAA (Taiwan), and KASI (Republic of Korea), in cooperation with the Republic of Chile. The Joint ALMA Observatory is operated by ESO, AUI/NRAO and NAOJ. M.L.R.v.t.H. acknowledges support from the Michigan Society of Fellows. M.L. acknowledges support from the Dutch Research Council (NWO) grant 618.000.001. J.J.T. acknowledges funding from NSF grant AST-1814762. The National Radio Astronomy Observatory is a facility of the National Science Foundation operated under cooperative agreement by Associated Universities, Inc. J.K.J. acknowledges support from the Independent Research Fund Denmark (grant No. 0135-00123B). E.A.B. acknowledges support from NSF AAG grant No. 1907653. Astrochemistry in Leiden is supported by the Netherlands Research School for Astronomy (NOVA).

Appendix A
Physical and Kinematical Structure of L1527

Figure A1 presents the velocity along the line of sight for the material in the disk and inner envelope midplane. The highest velocities are only reached in the inner disk, presenting an opportunity to study disk emission unaffected by the envelope. At intermediate velocities ($\Delta|v| \sim 1.6$–$2.6\,km\,s^{-1}$), redshifted emission from the envelope originates in front of the disk, while at blueshifted velocities we see the disk in front of the

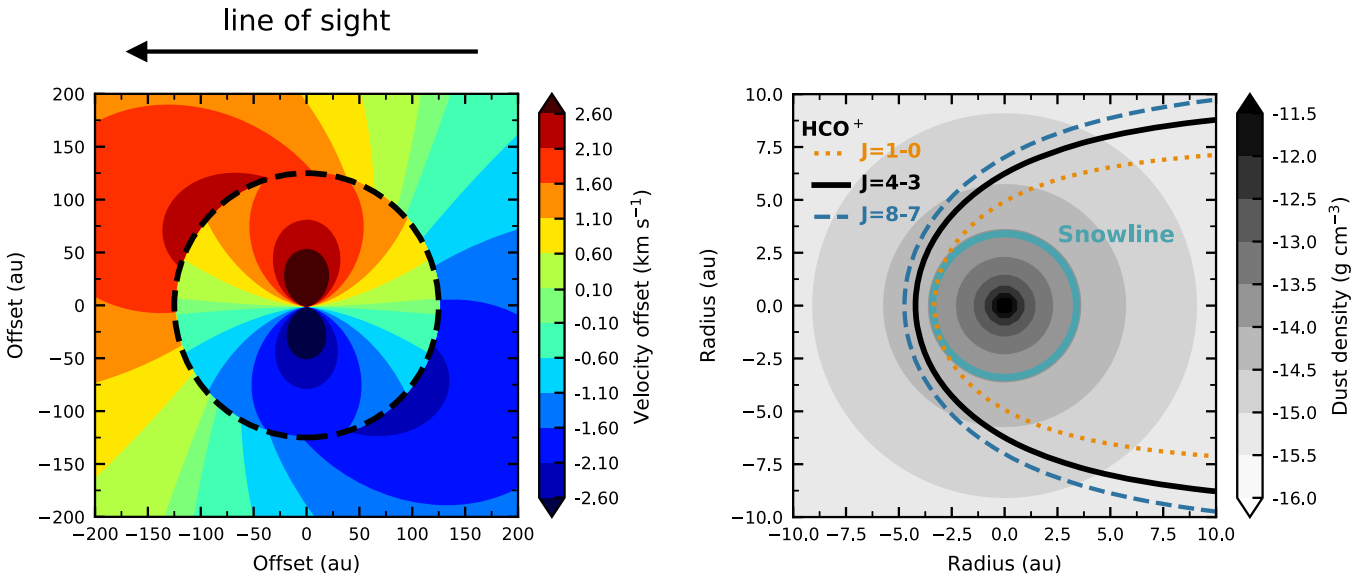

Figure A1. Left panel: face-on view of the midplane in the disk and inner envelope of L1527, showing the velocity component along the line of sight (the observer is on the left as indicated by the black arrow above the panel). The material in the 125 au disk (marked by a dashed line) has a Keplerian velocity, while the envelope material has a rotating infalling velocity profile (Ulrich 1976; Cassen & Moosman 1981). The adopted stellar mass is 0.4 $M_\odot$. Right panel: dust density in the inner 10 au and the $\tau = 1$ surfaces for the dust emission in our model at the wavelengths of the HCO$^+$ $J = 1 - 0$ (89.188523 GHz; dotted orange line), $J = 4 - 3$ (356.734288 GHz; solid black line), and $J = 8 - 7$ (713.342090 GHz; dashed blue line) transitions. The snowline at 3.4 au is indicated by the blue circle.

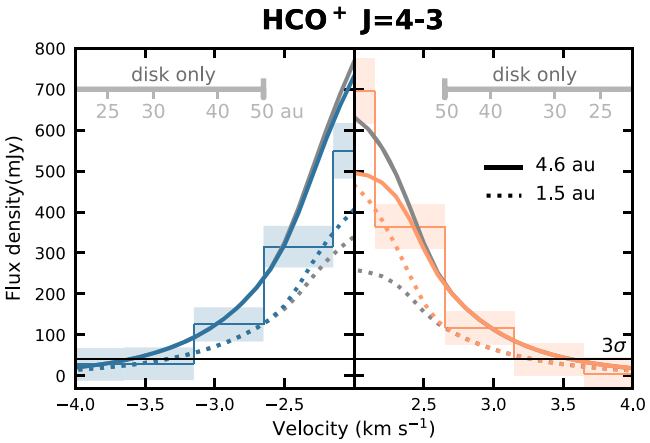

Figure A2. Spectra of the HCO$^+$ emission extracted in a 0.″75 aperture centered on the blueshifted emission peak (left) and on the redshifted emission peak (right). The observations are binned to 0.5 km s^{-1}, and the shaded area depicts the 3σ uncertainty and a 10% flux calibration uncertainty. The solid lines are for models with a snowline at 4.6 au, and the dotted lines are for models with a snowline at 1.5 au. For the colored lines the temperature factor required for that particular snowline location has only been applied to the disk, while for the gray lines this temperature factor has been applied to both disk and envelope. The difference between colored and gray lines is thus only the temperature in the envelope. The horizontal black line marks the 3σ level. The velocity range containing only emission from the disk is marked by gray bars in the top of the panels, and the maximum radius probed at certain velocities is indicated.

envelope. This can result in asymmetric line profiles, as, for example, in Figure 3, especially when the emission becomes optically thick. For HCO$^+$, we can illustrate this clearly by comparing models where the temperature modification as described in Section 5.1 is applied only to the disk or to both the disk and envelope. As can be seen in Figure A2, the blueshifted emission at velocities $\leqslant -2.0$ km s^{-1} is hardly affected by a change in envelope temperature, signaling that most of the emission is originating in the disk. The redshifted emission is more strongly affected, and the redshifted emission at velocities $\leqslant 2.5$ km s^{-1} thus has a strong envelope component. Another effect that comes into play at lower redshifted velocities is absorption due to the foreground infalling envelope. This effect, together with larger-scale emission being resolved out, may explain why the model better reproduces the blueshifted H^{13}CO$^+$ emission, as the convolution of the synthetic image cube does not capture the effects of the interferometer.

Figure A1 also shows the location where the dust emission becomes optically thick along the midplane (that is, along the north–south direction) in our model. We adopt a parameterized dust opacity with a value of 3.5 cm^2 g^{-1} at 850 μm and a spectral index β of 0.25 (Tobin et al. 2013). At the frequency of the HCO$^+$ $J = 4 - 3$ transition (356.734288 GHz; as observed), the dust becomes optically thick just outside the snowline. Even for the lowest HCO$^+$ transition ($J = 1 - 0$ at 89.188523 GHz) the snowline coincides with or falls just inside of the $\tau = 1$ surface and will be hidden by the dust.

The temperature and density structure in the adopted physical model for L1527 is shown in Figure A3. This model was derived by Tobin et al. (2013) using a large grid of 3D radiative transfer models to model the thermal dust emission in the (sub)millimeter, the scattered light L' image, and the multiwavelength SED. The model includes a rotating infalling envelope (Ulrich 1976; Cassen & Moosman 1981) and a flared disk (e.g., Hartmann et al. 1998). In addition to a protostellar luminosity of 1.0 $L_\odot$, a luminosity of 1.75 $L_\odot$ is used to account for the accretion from the disk onto the protostar.

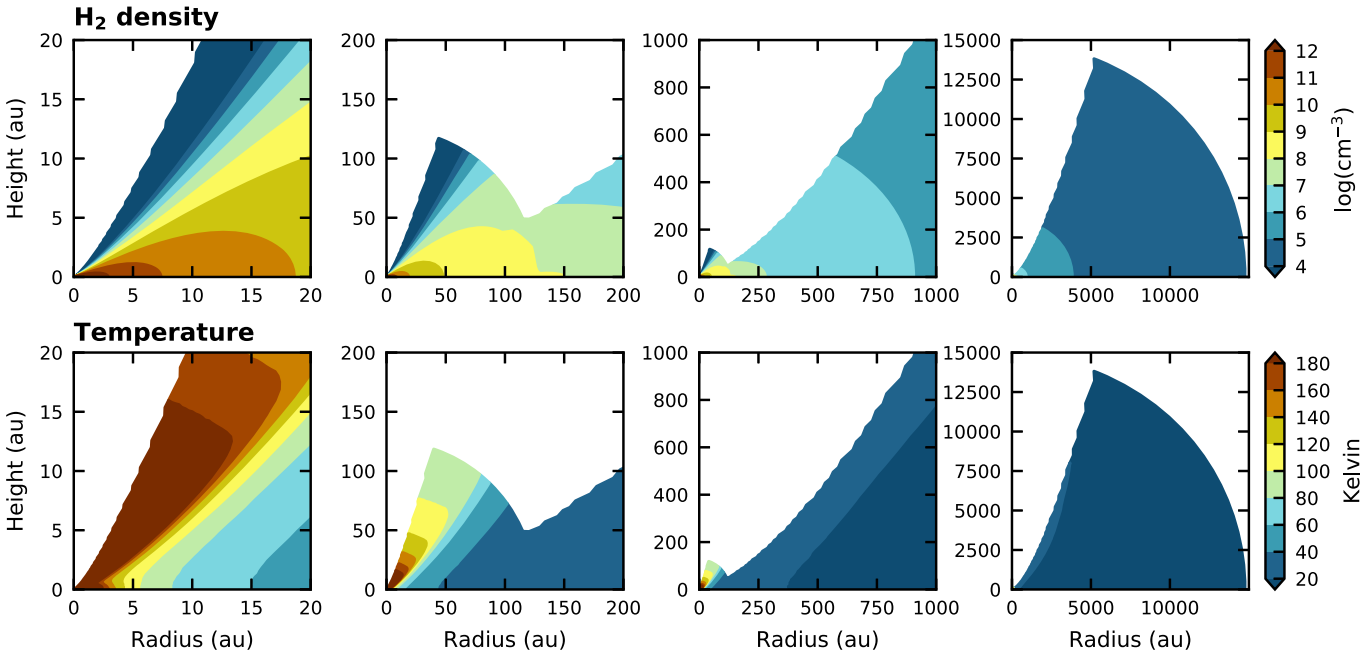

Figure A3. Density (top panels) and temperature (bottom panels) structure for the disk and envelope of L1527 from the best-fit model by Tobin et al. (2013). From left to right, panels display larger spatial scales. The disk outer radius is 125 au.

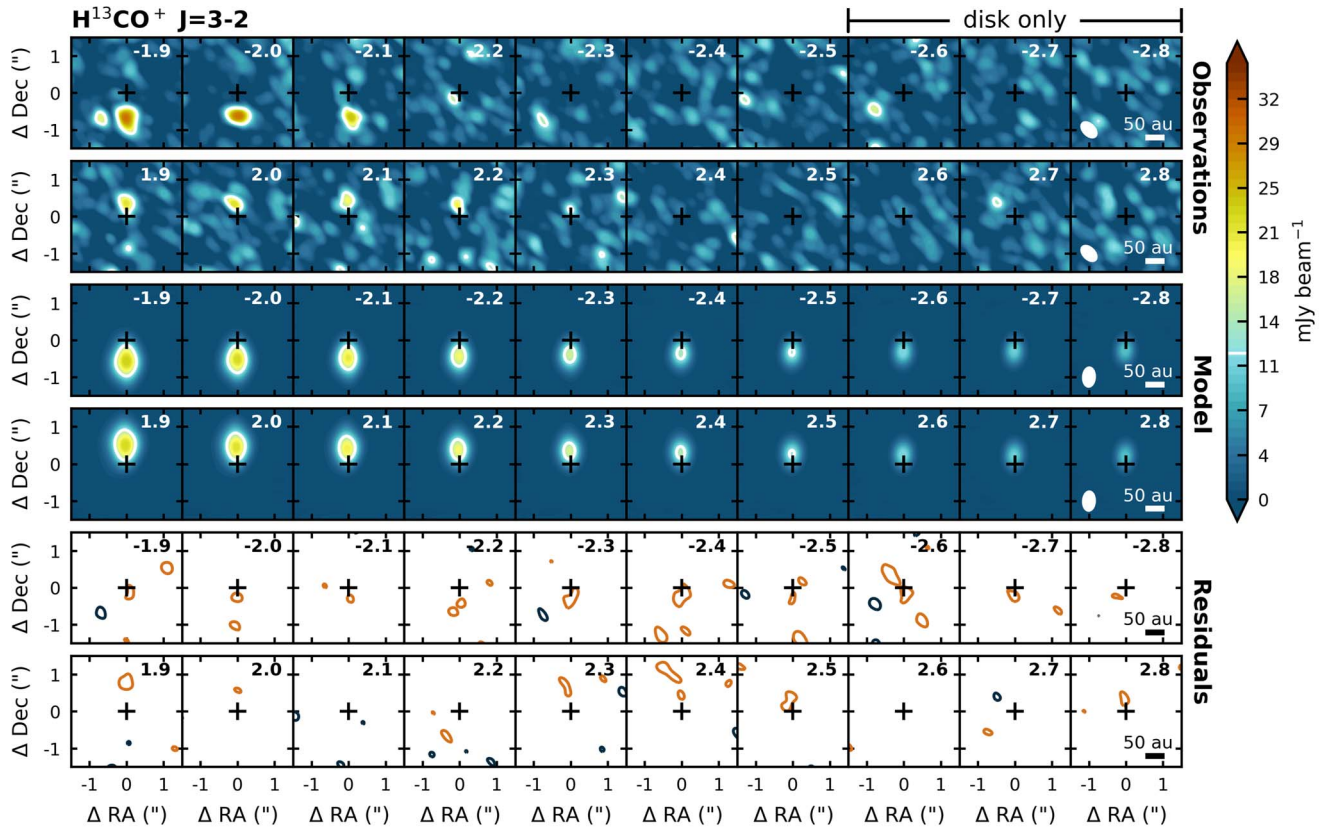

Figure B1. Same as Figure 2, but for $H^{13}CO^+$ emission. The model has a constant abundance of 3×10^{-12}. The depicted velocity range is slightly different from that shown for HCO^+ in Figure 2 because the $H^{13}CO^+$ emission is only detected at slightly lower velocities.

Appendix B
Parameterized Modeling of $H^{13}CO^+$ Emission

The $H^{13}CO^+$ observations can be reproduced by a constant abundance of 3×10^{-12}, as presented in Figure B1. This breaks the degeneracy between an HCO^+ model with an abundance of 2×10^{-11} at radii $\leqslant$60 au and an abundance of 2×10^{-10} at larger radii (as shown in Figure 2) and a model with an abundance of 2×10^{-11} in the entire 125 au disk and an

abundance of 1×10^{-9} in the envelope, as the $H^{13}CO^+$ observations are in better agreement with the former HCO^+ abundance structure.

Appendix C
Chemical Modeling of HCO^+ Emission

Figure C1 shows a schematic of the chemical network used to model HCO^+ and its relation with the water snowline using the physical structure of L1527, as shown in Figure A3. The chemistry is evolved for a duration of 10^5 yr, but, for comparison, Figure C2 shows the HCO^+ abundance for the fiducial initial conditions of $X(CO) = 10^{-4}$, $X(H_2O) = 10^{-6}$, and a CR rate of 10^{18} s^{-1} after 10^6 yr. The HCO^+ abundances after 10^5 yr but for different initial conditions are presented in Figures C3–C5: a low CO abundance of 10^{-6} (Figure C3), a high H_2O abundance of 10^{-4} (Figure C4), and a CR rate of 10^{17} s^{-1} (Figure C5).

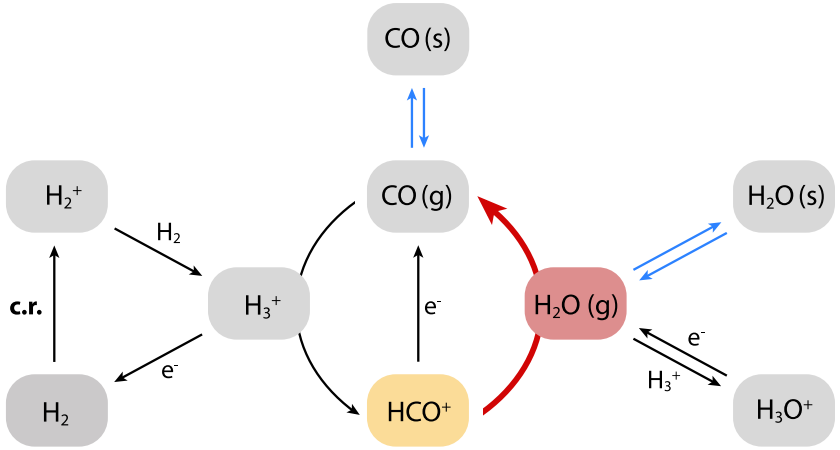

Figure C1. Schematic representation of the chemical network used to model HCO^+ (orange). The reaction responsible for the anticorrelation between HCO^+ and H_2O is highlighted with a red arrow. Freezeout and thermal desorption reactions are marked by blue arrows, where "g" denotes gas-phase species and "s" denotes ice species. Ionization of H_2 by CRs (c.r.) initiates the ion-neutral chemistry. Leemker et al. (2021) did not include the freezeout of CO because their disks were too warm for CO ice. Parameters that are adjusted in this work are the initial CO and H_2O abundances and the CR ionization rate.

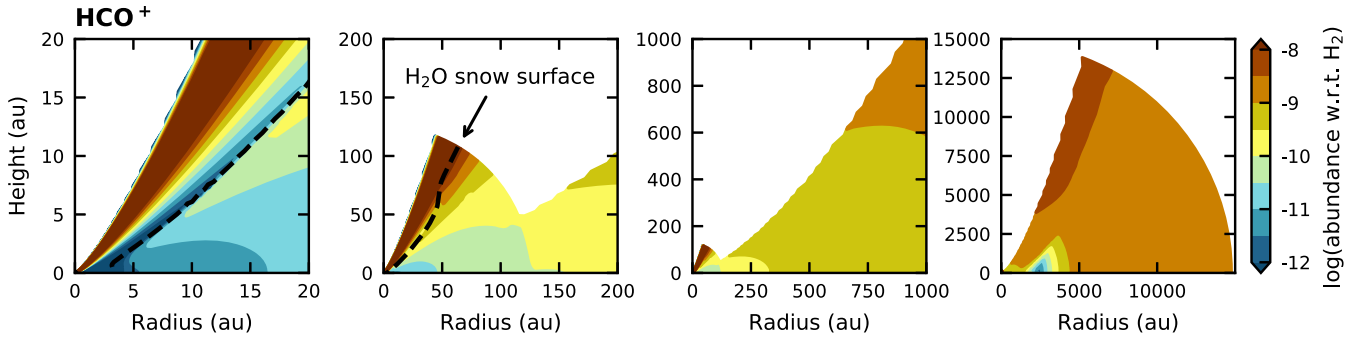

Figure C2. Abundance structure for HCO^+ for the fiducial model (initial CO and H_2O abundances of 10^{-4} and 10^{-6}, respectively, and a CR ionization rate of 10^{-18} s^{-1}) as shown in Figure 4, but after 10^6 yr instead of 10^5 yr. From left to right, panels display larger spatial scales. The disk outer radius is 125 au. The dashed line in the two leftmost columns marks the H_2O snow surface and the midplane snowline at 3.4 au.

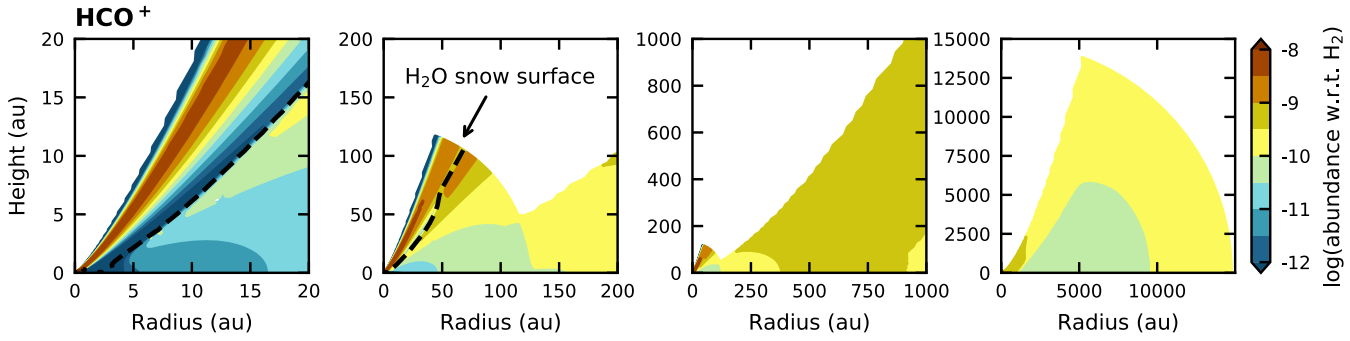

Figure C3. Abundance structure for HCO^+ as shown in Figure 4, but for a model with a lower initial CO abundance of 10^{-6}.

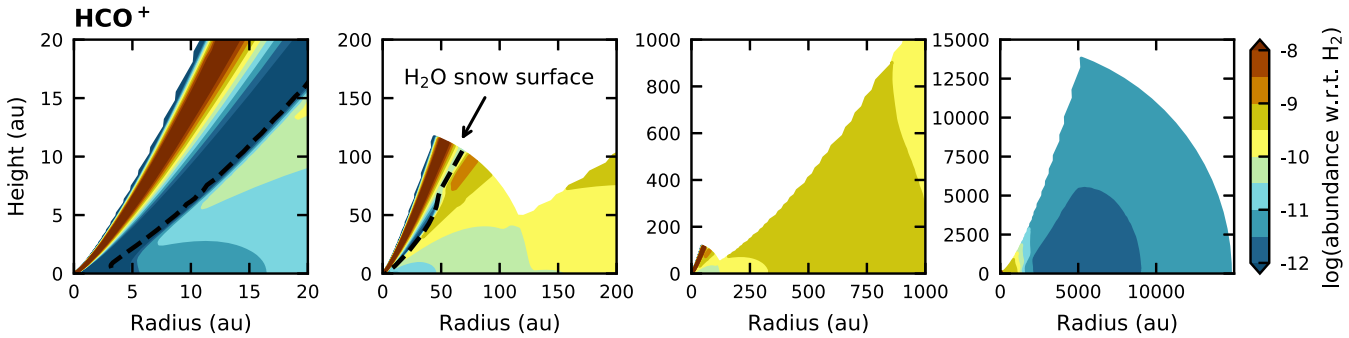

Figure C4. Abundance structure for HCO^+ as shown in Figure 4, but for a model with a higher initial H_2O abundance of 10^{-4}.

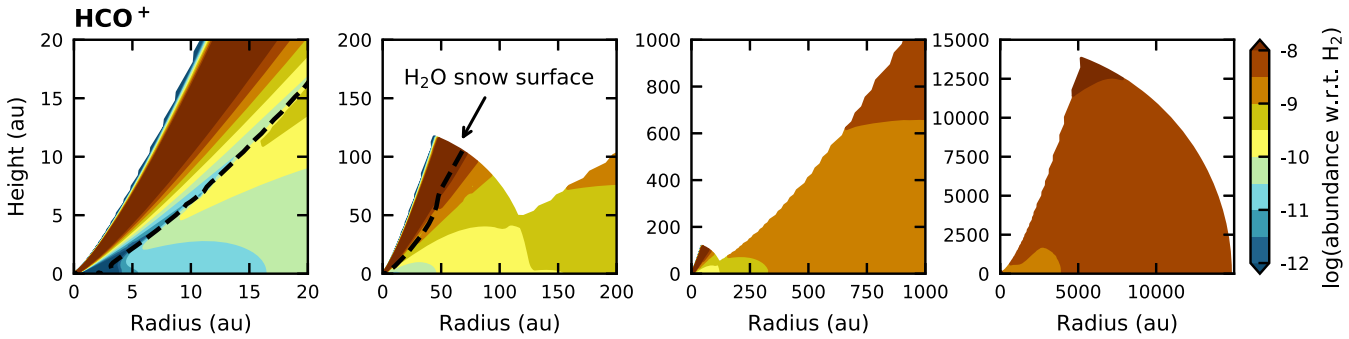

Figure C5. Abundance structure for HCO^+ as shown in Figure 4, but for a model with a canonical CR ionization rate of 10^{-17} s^{-1}.

ORCID iDs

Merel L. R. van 't Hoff https://orcid.org/0000-0002-2555-9869
Margot Leemker https://orcid.org/0000-0003-3674-7512
John J. Tobin https://orcid.org/0000-0002-6195-0152
Daniel Harsono https://orcid.org/0000-0001-6307-4195
Jes K. Jørgensen https://orcid.org/0000-0001-9133-8047
Edwin A. Bergin https://orcid.org/0000-0003-4179-6394

References

ALMA Partnership, Brogan, C. L., Pérez, L. M., et al. 2015, ApJL, 808, L3
Andrews, S. M., Huang, J., Pérez, L. M., et al. 2018, ApJL, 869, L41
Andrews, S. M., & Williams, J. P. 2005, ApJ, 631, 1134
Aso, Y., Ohashi, N., Aikawa, Y., et al. 2017, ApJ, 849, 56
Balbus, S. A., & Hawley, J. F. 1991, ApJ, 376, 214
Bergin, E. A., Melnick, G. J., & Neufeld, D. A. 1998, ApJ, 499, 777
Bisschop, S. E., Fraser, H. J., Öberg, K. I., van Dishoeck, E. F., & Schlemmer, S. 2006, A&A, 449, 1297
Bosman, A. D., Walsh, C., & van Dishoeck, E. F. 2018, A&A, 618, A182
Brinch, C., & Hogerheijde, M. R. 2010, A&A, 523, A25
Bryden, G., Chen, X., Lin, D. N. C., Nelson, R. P., & Papaloizou, J. C. B. 1999, ApJ, 514, 344
Cassen, P., & Moosman, A. 1981, Icar, 48, 353
Cleeves, L. I., Bergin, E. A., & Adams, F. C. 2014, ApJ, 794, 123
Cleeves, L. I., Bergin, E. A., Qi, C., Adams, F. C., & Öberg, K. I. 2015, ApJ, 799, 204
Collings, M. P., Dever, J. W., Fraser, H. J., McCoustra, M. R. S., & Williams, D. A. 2003, ApJ, 583, 1058
Davis, S. S. 2005, ApJ, 620, 994
Dong, R., Liu, S.-y., Eisner, J., et al. 2018, ApJ, 860, 124
Drążkowska, J., & Alibert, Y. 2017, A&A, 608, A92
Du, F., Bergin, E. A., Hogerheijde, M., et al. 2017, ApJ, 842, 98
Eistrup, C., Walsh, C., & van Dishoeck, E. F. 2016, A&A, 595, A83
Eistrup, C., Walsh, C., & van Dishoeck, E. F. 2018, A&A, 613, A14
Favre, C., López-Sepulcre, A., Ceccarelli, C., et al. 2017, A&A, 608, A82
Fraser, H. J., Collings, M. P., McCoustra, M. R. S., & Williams, D. A. 2001, MNRAS, 327, 1165
Gaches, B. A. L., & Offner, S. S. R. 2018, ApJ, 861, 87
Gaia Collaboration, Brown, A. G. A., Vallenari, A., et al. 2021, A&A, 649, A1
Gammie, C. F. 1996, ApJ, 457, 355
Garaud, P., & Lin, D. N. C. 2007, ApJ, 654, 606
Garrod, R. T., & Herbst, E. 2006, A&A, 457, 927
Green, J. D., Evans, N. J. I., Jørgensen, J. K., et al. 2013, ApJ, 770, 123
Gressel, O., Nelson, R. P., & Turner, N. J. 2012, MNRAS, 422, 1140
Güdel, M., Briggs, K. R., Arzner, K., et al. 2007, A&A, 468, 353
Harsono, D., Bjerkeli, P., van der Wiel, M. H. D., et al. 2018, NatAs, 2, 646
Harsono, D., Bruderer, S., & van Dishoeck, E. F. 2015, A&A, 582, A41
Harsono, D., Persson, M. V., Ramos, A., et al. 2020, A&A, 636, A26
Hartmann, L., Calvet, N., Gullbring, E., & D'Alessio, P. 1998, ApJ, 495, 385
Hsieh, T.-H., Murillo, N. M., Belloche, A., et al. 2019, ApJ, 884, 149
Jørgensen, J. K., Schöier, F. L., & van Dishoeck, E. F. 2004, A&A, 416, 603
Jørgensen, J. K., Schöier, F. L., & van Dishoeck, E. F. 2005, A&A, 435, 177
Jørgensen, J. K., Visser, R., Sakai, N., et al. 2013, ApJL, 779, L22
Karska, A., Kaufman, M. J., Kristensen, L. E., et al. 2018, ApJS, 235, 30
Kataoka, A., Muto, T., Momose, M., Tsukagoshi, T., & Dullemond, C. P. 2016, ApJ, 820, 54
Kataoka, A., Muto, T., Momose, M., et al. 2015, ApJ, 809, 78
Krolikowski, D. M., Kraus, A. L., & Rizzuto, A. C. 2021, AJ, 162, 110
Kruijer, T. S., Burkhardt, C., Budde, G., & Kleine, T. 2017, PNAS, 114, 6712
Kwon, W., Looney, L. W., Mundy, L. G., Chiang, H.-F., & Kemball, A. J. 2009, ApJ, 696, 841
Lecar, M., Podolak, M., Sasselov, D., & Chiang, E. 2006, ApJ, 640, 1115
Leemker, M., van 't Hoff, M. L. R., Trapman, L., et al. 2021, A&A, 646, A3
Leya, I., Schönbächler, M., Wiechert, U., Krähenbühl, U., & Halliday, A. N. 2008, E&PSL, 266, 233
Lichtenberg, T., Drążkowska, J., Schönbächler, M., Golabek, G. J., & Hands, T. O. 2021, Sci, 371, 365
Mathews, G. S., Klaassen, P. D., Juhász, A., et al. 2013, A&A, 557, A132
McElroy, D., Walsh, C., Markwick, A. J., et al. 2013, A&A, 550, A36
McMullin, J. P., Waters, B., Schiebel, D., Young, W., & Golap, K. 2007, in ASP Conf. Ser. 376, Astronomical Data Analysis Software and Systems XVI, ed. R. A. Shaw, F. Hill, & D. J. Bell (San Francisco, CA: ASP), 127
Milam, S. N., Savage, C., Brewster, M. A., Ziurys, L. M., & Wyckoff, S. 2005, ApJ, 634, 1126
Notsu, S., Akiyama, E., Booth, A., et al. 2019, ApJ, 875, 96
Notsu, S., Nomura, H., Walsh, C., et al. 2018, ApJ, 855, 62
Notsu, S., van Dishoeck, E. F., Walsh, C., Bosman, A. D., & Nomura, H. 2021, A&A, 650, A180
Öberg, K. I., Murray-Clay, R., & Bergin, E. A. 2011, ApJL, 743, L16
Ohashi, N., Hayashi, M., Ho, P. T. P., & Momose, M. 1997, ApJ, 475, 211
Oka, A., Nakamoto, T., & Ida, S. 2011, ApJ, 738, 141
Oya, Y., Sakai, N., Lefloch, B., et al. 2015, ApJ, 812, 59

Padovani, M., Hennebelle, P., Marcowith, A., & Ferrière, K. 2015, A&A, 582, L13
Padovani, M., Ivlev, A. V., Galli, D., & Caselli, P. 2018, A&A, 614, A111
Padovani, M., Marcowith, A., Hennebelle, P., & Ferrière, K. 2016, A&A, 590, A8
Phillips, T. G., van Dishoeck, E. F., & Keene, J. 1992, ApJ, 399, 533
Sakai, N., Oya, Y., Sakai, T., et al. 2014, ApJL, 791, L38
Schmalzl, M., Visser, R., Walsh, C., et al. 2014, A&A, 572, A81
Schöier, F. L., van der Tak, F. F. S., van Dishoeck, E. F., & Black, J. H. 2005, A&A, 432, 369
Schoonenberg, D., & Ormel, C. W. 2017, A&A, 602, A21
Schwarz, K. R., Bergin, E. A., Cleeves, L. I., et al. 2019, ApJ, 877, 131
Segura-Cox, D. M., Schmiedeke, A., Pineda, J. E., et al. 2020, Natur, 586, 228
Seifert, R. A., Cleeves, L. I., Adams, F. C., & Li, Z.-Y. 2021, ApJ, 912, 136
Sheehan, P. D., Tobin, J. J., Federman, S., Megeath, S. T., & Looney, L. W. 2020, ApJ, 902, 141
Shirley, Y. L., Mason, B. S., Mangum, J. G., et al. 2011, AJ, 141, 39
Stevenson, D. J., & Lunine, J. I. 1988, Icar, 75, 146
Tobin, J. J., Hartmann, L., Calvet, N., & D'Alessio, P. 2008, ApJ, 679, 1364
Tobin, J. J., Hartmann, L., Chiang, H.-F., et al. 2012, Natur, 492, 83
Tobin, J. J., Hartmann, L., Chiang, H.-F., et al. 2013, ApJ, 771, 48
Trinquier, A., Elliott, T., Ulfbeck, D., et al. 2009, Sci, 324, 374
Tsukamoto, Y., Machida, M. N., & Inutsuka, S.-i. 2021, ApJL, 920, L35
Tychoniec, Ł., Manara, C. F., Rosotti, G. P., et al. 2020, A&A, 640, A19
Ulrich, R. K. 1976, ApJ, 210, 377
Umebayashi, T., & Nakano, T. 1980, PASJ, 32, 405
Umebayashi, T., & Nakano, T. 1981, PASJ, 33, 617
Umebayashi, T., & Nakano, T. 2009, ApJ, 690, 69
van der Tak, F. F. S., Lique, F., Faure, A., Black, J. H., & van Dishoeck, E. F. 2020, Atoms, 8, 15
van 't Hoff, M. L. R., Harsono, D., Tobin, J. J., et al. 2020, ApJ, 901, 166
van 't Hoff, M. L. R., Harsono, D., van Gelder, M. L., et al. 2022, ApJ, 924, 5
van 't Hoff, M. L. R., Persson, M. V., Harsono, D., et al. 2018a, A&A, 613, A29
van 't Hoff, M. L. R., Tobin, J. J., Harsono, D., & van Dishoeck, E. F. 2018b, A&A, 615, A83
van 't Hoff, M. L. R., Walsh, C., Kama, M., Facchini, S., & van Dishoeck, E. F. 2017, A&A, 599, A101
Visser, R., Kristensen, L. E., Bruderer, S., et al. 2012, A&A, 537, A55
Whitney, B. A., Wood, K., Bjorkman, J. E., & Wolff, M. J. 2003, ApJ, 591, 1049
Yang, H., Li, Z.-Y., Looney, L. W., et al. 2016, MNRAS, 460, 4109
Zhou, S., Evans, N. J. I., & Wang, Y. 1996, ApJ, 466, 296
Zhu, Z., Stone, J. M., Rafikov, R. R., & Bai, X.-n. 2014, ApJ, 785, 122